



OPEN

# Influence of proton irradiation on the magnetic properties of two-dimensional Ni(II) molecular magnet

Dominik Czernia<sup>1</sup>✉, Piotr Konieczny<sup>1</sup>✉, Ewa Juszyńska-Gałązka<sup>1,2</sup>, Marcin Perzanowski<sup>1</sup>, Janusz Lekki<sup>1</sup>, Anabel Berenice González Guillén<sup>3</sup> & Wiesław Łasocha<sup>3</sup>

The influence of 1.9 MeV proton irradiation on structural and magnetic properties has been explored in the two-dimensional (2D)  $\text{NiSO}_4(1,3\text{-phenylenediamine})_2$  coordination ferrimagnet. The X-ray powder diffraction and IR spectroscopy revealed that the octahedrons with Ni ion in the center remain unchanged regardless of the fluence a sample received. In contrast, proton irradiation greatly influences the hydrogen bonds in the flexible parts in which the 1,3-phenylenediamine is involved. Dc magnetic measurements revealed that several magnetic properties were modified with proton irradiation. The isothermal magnetization measured at  $T = 2.0$  K varied with the proton dose, achieving a 50% increase in magnetization in the highest measured field  $\mu_0 H_{dc} = 7$  T or a 25% decrease in remanence. The most significant change was observed for the coercive field, which was reduced by 90% compared to the non-irradiated sample. The observed results are accounted for the increased freedom of magnetic moments rotation and the modification of intralayer exchange couplings.

The recent intensive investigations in the field of multifunctional molecular materials are integrally related to their possible application in modern technology, such as high-density data storage and processing<sup>1–4</sup>, magnetic refrigeration<sup>5–8</sup>, or optically active sensors and switches<sup>9,10</sup>. The broad capability of molecular magnetism emerges from the variety of available structures<sup>11,12</sup> and the possibility of changing their properties with external stimuli, including temperature, pressure<sup>13</sup>, and light irradiation<sup>14</sup>. Proton irradiation is another approach for tuning material properties by external factors. It is currently widely employed in the studies of carbon allotropes<sup>15,16</sup>, semiconductors<sup>17</sup>, films<sup>18</sup>, superconductors<sup>19</sup>, and alloys<sup>20</sup> to engineer material features in a controllable manner<sup>21–24</sup>. Solids irradiated with energetic particles are exposed to extremely high-density local energy deposition that causes nonlinear and threshold effects<sup>25</sup>. As a result, new materials with novel properties can be obtained.

In particular, ion irradiation is used to modify magnetic properties. The induced defects may give rise to paramagnetic response in non-magnetic materials when the defect concentration exceeds a specific threshold value<sup>26–28</sup> or alter the magnetic properties of paramagnets and systems with long-range magnetic order (LRMO), especially when strong magnetostructural correlations are present. The irradiation can increase Curie temperature<sup>29–31</sup> and impact such properties as the coercive field, magnetization saturation, g-factor, and shape of the magnetic hysteresis loop<sup>32–34</sup>. Proton irradiation can generate changes at the atomic level over the selected area and depth by adjusting protons energy, which makes this approach perspective for the controlled engineering of magnetic materials<sup>29</sup>.

Currently, there are no systematic studies on the response of molecular magnetic materials to ion irradiation. To fill this gap, we examined the effects of 1.9 MeV proton irradiation on the magnetic properties of the  $\text{NiSO}_4(1,3\text{-phenylenediamine})_2$  coordination polymer, hereafter abbreviated as  $\text{Ni(MPD)}_2\text{SO}_4$ . This molecular magnet reveals a considerable size of the coercive field and long-range magnetic ordering below  $T_C = 24$  K. X-ray powder diffraction, infrared spectroscopy, and magnetic measurements were performed to investigate the influence of proton fluence  $\phi = 5 \times 10^{13} - 2.2 \times 10^{15} \text{ cm}^{-2}$  on structural and magnetic properties. Although structural changes were observed only within the polymer part related to the C–H and N–H bonds, the proton

<sup>1</sup>Institute of Nuclear Physics PAN, ul. Radzikowskiego 152, 31-342 Cracow, Poland. <sup>2</sup>Research Center for Thermal and Entropic Science, Graduate School of Science, Osaka University, 1-1 Machikaneyamacho, Toyonaka, Osaka 560-0043, Japan. <sup>3</sup>Faculty of Chemistry, Jagiellonian University, ul. Gronostajowa 2, 30-387 Cracow, Poland. ✉email: dominik.czernia@ifj.edu.pl; piotr.konieczny@ifj.edu.pl

irradiation has induced significant modifications of magnetic properties, especially the coercive field, degree of irreversibility, and maximum magnetization.

## Results

**X-ray powder diffraction (XRPD).** The  $\text{Ni}(\text{MPD})_2\text{SO}_4$  (Fig. 1) crystallizes in a monoclinic crystal system ( $Cc$  space group). The nickel (II) ions are bridged by tetrahedral  $\text{SO}_4^{2-}$  anions forming 2D layers parallel to the  $bc$  plane, and each layer is separated from one another by the 1,3-phenylenediamine (MPD) ligand. The nickel atom occupies the center of a distorted octahedron formed by two nitrogen atoms from the diamine molecules (MPD) and four oxygen atoms from three  $\text{SO}_4^{2-}$  anions. Each  $\text{Ni}^{2+}$  possesses six  $\text{Ni}^{2+}$  nearest neighbors and is separated from them by a distance of 4.914 Å, 4.931 Å, or 6.546 Å (two of each). The interlayer Ni–Ni distance is equal to 14.559 Å. More details regarding  $\text{Ni}(\text{MPD})_2\text{SO}_4$  structure were described in<sup>35</sup>. The XRPD measurements of all samples have not shown meaningful changes in the diffraction patterns pointing to the conservation of the  $\text{Ni}(\text{MPD})_2\text{SO}_4$  core structure after proton irradiation (see Supplementary Information Figure S1 online). However, greater half-widths of the diffraction peaks after proton irradiation may indicate the increase in crystal lattice microstrains or crystallites size reduction.

**Infrared spectroscopy (IR).** In the mid-infrared range, the absorption spectra observed for  $\text{Ni}(\text{MPD})_2\text{SO}_4$ , for samples irradiated with various fluences, have complex character (see Fig. 2). In the range of the deformation vibrations ( $\nu < 2000 \text{ cm}^{-1}$ ), a series of  $\delta_{\text{C-H}}$  bands (in a ring), overlapping with those originating from  $\text{SO}_4$  ions,

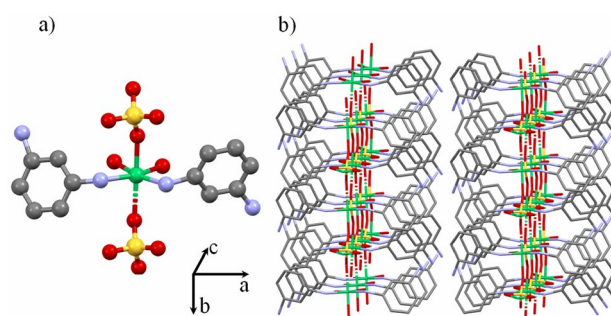


**Figure 1.** The crystal structure of  $\text{Ni}(\text{MPD})_2\text{SO}_4$ : (a) representative molecular fragment (b) packing. Colors: Ni (green), S (yellow), O (red), C (black), N (light blue). Hydrogen atoms are omitted for clarity.

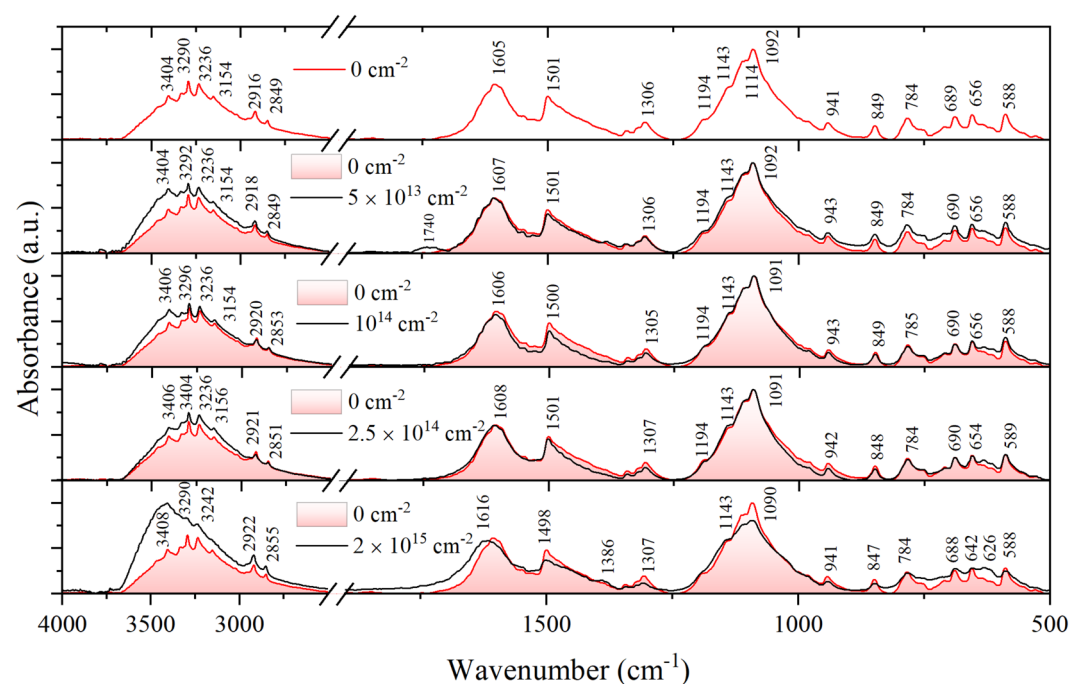


**Figure 2.** Fourier-transform infrared spectroscopy (FTIR) patterns of the  $\text{Ni}(\text{MPD})_2\text{SO}_4$  samples irradiated with various fluences.

are visible. The IR spectra show  $\text{NiSO}_4$  sharp peaks of the characteristic S–O stretch [ $\nu_{\text{S-O}}(\text{SO}_4)$  900–1500  $\text{cm}^{-1}$ ] and deformation [ $\delta_{\text{S-O}}(\text{SO}_4)$  400–700  $\text{cm}^{-1}$ ] vibrations. On the other hand, a band corresponding to the stretching vibration from the Ni=O group is visible at about 600  $\text{cm}^{-1}$ . Broad bands, corresponding to S–O vibrations in the  $\text{SO}_4$  atomic group, were observed at about: ~525  $\text{cm}^{-1}$  as  $\delta_{\text{S-O}}$  deformation vibrations, and ~1100  $\text{cm}^{-1}$  and ~1600  $\text{cm}^{-1}$  as  $\nu_{\text{S-O}}$  stretching vibrations<sup>36</sup>.

Vibration bands of the lighter atoms, i.e., C–H and N–H in MPD ligand, both deforming, i.e., in the range of 500–2000  $\text{cm}^{-1}$ , and the range of stretching vibrations, i.e., above 2000  $\text{cm}^{-1}$ , strongly overlap with the vibrations of the groups containing heavy atoms. They are visible in the form of low-intensity bands emerging from wide bands corresponding to the vibrations of the group, e.g.,  $\text{SO}_4$ . Bands at about (~700, ~1551)  $\text{cm}^{-1}$  are assigned to the vibrations of the CN group<sup>37</sup>.

The range of stretching vibrations deserves special attention. The broad band in this range ( $\nu_{\text{CH}}$ ,  $\nu_{\text{NH}}$ ) becomes asymmetric with the increase of the irradiation dose. The band is shifted towards a higher wavenumber (blue shift) which means that the strengths of the C–H and N–H are weakened<sup>38</sup>. The C–H and N–H bonds are involved well in forming hydrogen bonds, and the molecule's structure (shown in Fig. 1) perfectly enables it. A substantial change in the shape of the band with increasing irradiation dose proves the considerable influence of the hydrogen bonds on the ordering of the structure in its flexible parts in which MPD is involved.

Moreover, the visible asymmetry of the band indicates that there are different types of hydrogen bonds in which the nitrogen atom is involved. The nitrogen atom from the molecule's core (close to the nickel atom) is very stable (rigid) due to its involvement in covalent bonds. In contrast, the steric conditions for the "free" nitrogen atom favor the rapid formation/breaking of intermolecular bonds. Therefore, these weak interactions only affect the elastic part of the molecules, while the core of the molecule does not feel their presence. The assignments of major vibrational bands in the FTIR spectra of the  $\text{Ni}(\text{MPD})_2\text{SO}_4$  samples irradiated with various fluences are in Table 1.

**Magnetic properties.** The general magnetic properties of  $\text{Ni}(\text{MPD})_2\text{SO}_4$  were investigated in the recent work by González Guillén et al.<sup>35</sup>. Three magnetic couplings were found in the system: two competing intralayer superexchange pathways, antiferromagnetic and ferromagnetic, that lead to non-collinear ordering within a layer and a dipole–dipole coupling between layers. The low anisotropy of Ni(II) ions does not promote 2D long-range magnetic ordering (LRMO). Therefore, the LRMO occurs below the Curie temperature  $T_c = 24$  K when all three interactions (where the dipolar coupling is the weakest one) are strong enough to couple magnetic moments in 3D. The product of molar magnetic susceptibility and temperature  $\chi T$  of  $\text{Ni}(\text{MPD})_2\text{SO}_4$  measured

Wavenumber ( $\text{cm}^{-1}$ )					Assignment
0 ( $\text{cm}^{-2}$ )	$5 \times 10^{13}$ ( $\text{cm}^{-2}$ )	$10^{14}$ ( $\text{cm}^{-2}$ )	$2.5 \times 10^{14}$ ( $\text{cm}^{-2}$ )	$2.2 \times 10^{15}$ ( $\text{cm}^{-2}$ )	
3404	3404	3406	3406	3408	$\nu_{\text{N-H}}$ (of free amines)
			3404		
3290	3292	3296		3290	
3236	3236	3236	3236	3242	
3154	3154	3154	3156		$\nu_{\text{C-H}}$ (in ring)
2916	2918		2921	2922	$\nu_{\text{C-H}}$ (in $\text{CH}_2$ )
2849	2849	2853	2851	2855	$\nu_{\text{C-H}}$ (in $\text{CH}_2$ )
	1740				
1605	1607	1606	1608	1616	$\delta_{\text{N-H}}$ (rocking vibrations)
1501	1501	1500	1501		
				1498	$\nu_{\text{CN}}$
				1386	$\nu_{\text{Ni-S}}$
1306	1306	1305	1307	1307	$\delta_{\text{C-H}}$
1194	1194	1194	1194		$\delta_{\text{C-C}}$
1143	1143	1143	1143	1143	$\delta_{\text{C-C}}$
1114	1114	1114	1114	1114	$\nu_{\text{SO}_4^-}$
1092	1092	1091	1091	1090	$\nu_{\text{SO}_4^-}$
941	943	943	942	941	$\delta_{\text{S-O}} + \delta_{\text{C-H}}$
849	849	849	848	847	$\delta_{\text{S-O}} + \delta_{\text{C-H}}$
784		785	784	784	$\delta_{\text{S-O}} + \delta_{\text{C-H}}$
689	690	690	690	688	$\delta_{\text{S-O}} + \delta_{\text{C-H}}$
656	656	656	654	642	$\delta_{\text{S-O}} + \delta_{\text{C-H}}$
				626	$\delta_{\text{S-O}} + \delta_{\text{C-H}}$
588	588	588	589	588	$\delta_{\text{S-O}} + \nu_{\text{C-N}} + \delta_{\text{C-H}}$

**Table 1.** Assignment of major vibrational bands in the FTIR spectra of the  $\text{Ni}(\text{MPD})_2\text{SO}_4$  samples irradiated with various fluences<sup>36–38</sup>.

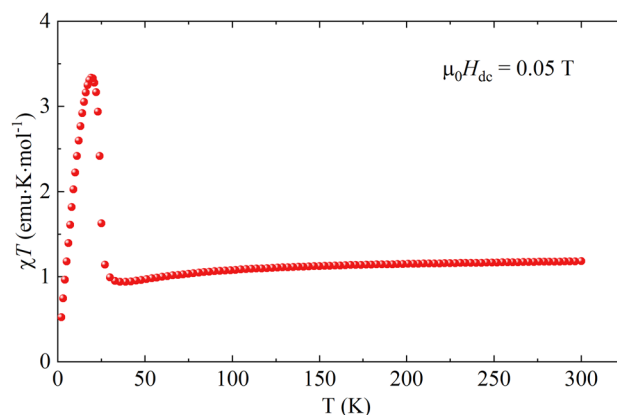


**Figure 3.** Temperature dependence of  $\chi T$  product for  $\text{Ni}(\text{MPD})_2\text{SO}_4$  reference sample in the static magnetic field of  $\mu_0 H_{\text{dc}} = 0.05$  T.

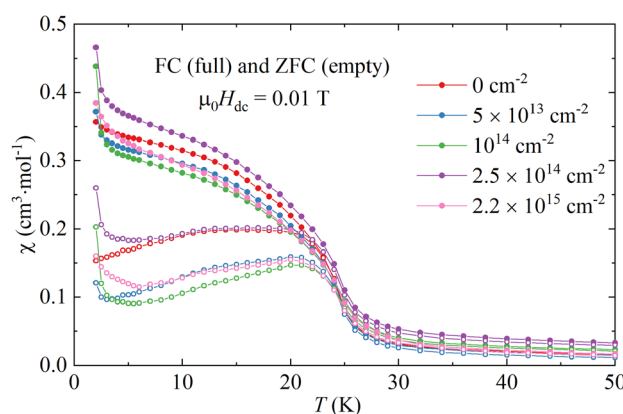


**Figure 4.** Field cooling (FC—full points) and zero-field cooling (ZFC—empty points) magnetic susceptibilities of  $\text{Ni}(\text{MPD})_2\text{SO}_4$  samples irradiated with various fluences  $\phi$  measured in static magnetic field  $\mu_0 H_{\text{dc}} = 0.01$  T at  $T = 2.0$ – $50$  K.

in the temperature range  $T = 2.0$ – $300$  K in a constant magnetic field of  $\mu_0 H_{\text{dc}} = 0.05$  T is shown in Fig. 3. At  $T = 300$  K,  $\chi T$  equals  $1.18 \text{ emu}\cdot\text{K}\cdot\text{mol}^{-1}$ , which can be obtained for a single isolated  $\text{Ni}^{\text{II}}$  ion with spin  $S_{\text{Ni}} = 1$ , assuming a spectroscopic factor  $g = 2.17$ . Such enhancement of  $g$  is expected for the  $\text{Ni}^{\text{II}}$  ion placed in the octahedral ligand field<sup>39</sup>.

The field cooling (FC) and zero-field cooling (ZFC) magnetic susceptibilities of  $\text{Ni}(\text{MPD})_2\text{SO}_4$  as a function of temperature are shown in Fig. 4 for proton fluences ranging from  $\phi = 0 \text{ cm}^{-2}$  to  $\phi = 2.2 \times 10^{15} \text{ cm}^{-2}$ . The temperature of phase transition to LRMO obtained from the temperature derivatives of FC and ZFC curves was  $T_{\text{C}} = 24$  K regardless of the sample radiation dosage. Compared to the reference sample, an additional increase in susceptibility was observed at the lowest temperatures for the samples irradiated with protons. However, the overall shapes of FC/ZFC were preserved above about  $T = 5.0$  K. The obtained susceptibility magnitude varied between each sample; for the FC mode, from 90 to 130% of the reference sample's corresponding value, whereas for ZFC, it varied between 55 and 170%. The largest FC/ZFC signal was obtained for  $\phi = 2.5 \times 10^{14} \text{ cm}^{-2}$  and the lowest for  $\phi = 10^{14} \text{ cm}^{-2}$ . The former sample was also the only one for which the FC/ZFC values above  $T = 5.0$  K were greater than the values for the reference sample.

The pair of ZFC and FC curves coincide with each other only above a certain irreversibility temperature  $T_{\text{irr}}$ <sup>40</sup>, which can be found by plotting the difference between FC,  $\chi_{\text{FC}}(T)$ , and ZFC,  $\chi_{\text{ZFC}}(T)$ , susceptibilities, and determining the temperature above which the difference becomes less than 5%. The degree of irreversibility  $\Delta\chi_{\text{irr}}$  was estimated for each studied fluence using the following integral<sup>41</sup>:

$$\Delta\chi_{\text{irr}} = \int_{T_1}^{T_2} (\chi_{\text{FC}}(T) - \chi_{\text{ZFC}}(T)) dT, \quad (1)$$

where  $T_1 = 2.0$  K and  $T_2 = T_{\text{irr}}$ .

The  $T_{\text{irr}}$  and  $\Delta\chi_{\text{irr}}$  are summarized in Fig. 5 for each irradiation dose. The  $T_{\text{irr}}$  weakly depends on the irradiation dose revealing values between 23 and 25 K, corresponding to 105–115% of the reference sample's  $T_{\text{irr}}$ .

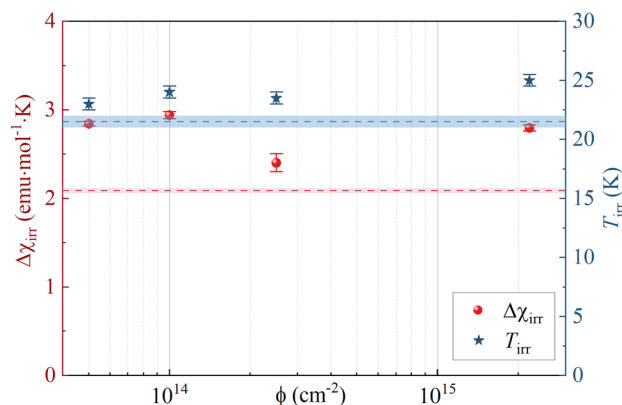


**Figure 5.** The degree of irreversibility  $\Delta\chi_{\text{irr}}$  (1) (left axis) and irreversibility temperature  $T_{\text{irr}}$  (right axis) for  $\text{Ni}(\text{MPD})_2\text{SO}_4$  samples irradiated with various fluences. The dashed lines represent the values obtained for the reference sample  $\phi = 0 \text{ cm}^{-2}$  and dotted areas their errors.

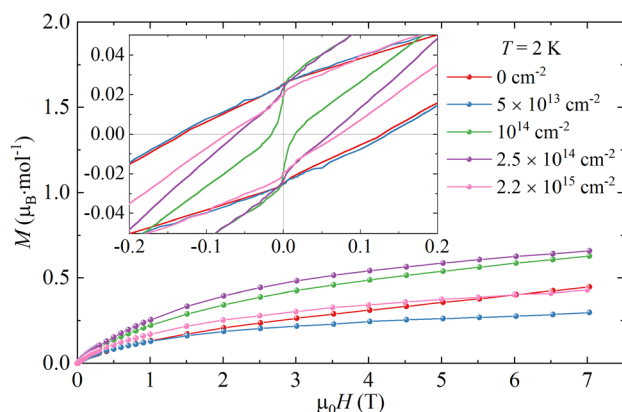


**Figure 6.** The isothermal magnetization of  $\text{Ni}(\text{MPD})_2\text{SO}_4$  samples irradiated with various fluences  $\phi$  measured at  $T = 2.0 \text{ K}$  and in applied magnetic fields from zero to  $\mu_0 H = 7 \text{ T}$ . Inset: the picture enlarged on  $\mu_0 H = [-0.2 \text{ T}, 0.2 \text{ T}]$  range to show the coercivity and remanence of the samples.

However, proton irradiation has a stronger influence on the degree of irreversibility. The obtained values of  $\Delta\chi_{\text{irr}}$  between  $2.4 \text{ emu}\cdot\text{mol}^{-1}\cdot\text{K}$  and  $2.95 \text{ emu}\cdot\text{mol}^{-1}\cdot\text{K}$ , are from 115 to 140% of the reference sample's  $\Delta\chi_{\text{irr}}$ . The highest  $T_{\text{irr}} = 25 \text{ K}$  was found for  $\phi = 2.2 \times 10^{15} \text{ cm}^{-2}$ , while the maximal value of  $\Delta\chi_{\text{irr}} = 2.95 \text{ emu}\cdot\text{mol}^{-1}\cdot\text{K}$  was for  $\phi = 10^{14} \text{ cm}^{-2}$ .

The Fig. 6 shows the isothermal magnetization of  $\text{Ni}(\text{MPD})_2\text{SO}_4$  obtained at  $T = 2.0 \text{ K}$  for all studied fluences  $\phi$ . In  $\mu_0 H = 7 \text{ T}$ , the lowest value of magnetization  $M_{7\text{T}} = 0.3 \mu_{\text{B}}\cdot\text{mol}^{-1}$  was observed for  $\phi = 5 \times 10^{13} \text{ cm}^{-2}$  sample and the highest  $M_{7\text{T}} = 0.65 \mu_{\text{B}}\cdot\text{mol}^{-1}$  for  $\phi = 5 \times 10^{14} \text{ cm}^{-2}$  sample, compared to  $M_{7\text{T}} = 0.45 \mu_{\text{B}}\cdot\text{mol}^{-1}$  for the reference sample (where  $M_{7\text{T}}$  is the magnetization at  $\mu_0 H = 7 \text{ T}$ ).

The low field part of magnetic hysteresis loops is depicted in the inset of Fig. 6, enlarged on the coercivity  $\mu_0 H_c$  and remanence  $M_R$ . The  $M(H)$  loops were opened below  $\mu_0 H = 1 \text{ T}$  for all the samples. The hysteresis loop for the sample with the lowest fluence of  $\phi = 5 \times 10^{13} \text{ cm}^{-2}$  coincided with the reference's loop in the field range  $\mu_0 H = [-1 \text{ T}, 1 \text{ T}]$ . For the remaining samples, the values of  $\mu_0 H_c$  and  $M_R$  were reduced, and a step in the  $M(H)$  loop near  $\mu_0 H = 0 \text{ T}$  appeared, which is especially visible for  $\phi = 10^{14} \text{ cm}^{-2}$ . Figure 7. shows the hysteresis loop parameters for the irradiated samples, presented as a relative value to the reference sample's coercivity ( $\mu_0 H_c = 0.13 \text{ T}$ ), remanence ( $M_R = 0.45 \mu_{\text{B}}\cdot\text{mol}^{-1}$ ), and magnetization at  $\mu_0 H = 7 \text{ T}$  ( $M_{7\text{T}} = 0.3 \mu_{\text{B}}\cdot\text{mol}^{-1}$ ).  $M_{7\text{T}}$  is reduced for  $\phi = 5 \times 10^{13} \text{ cm}^{-2}$  to 65% of the reference level, but it raises with an increasing  $\phi$  to 150% for  $\phi = 2.5 \times 10^{14} \text{ cm}^{-2}$ . The further increase in fluence reduces the value of  $M_{7\text{T}}$ , which becomes 95% of the reference level for the sample with the highest studied fluence of  $\phi = 2.2 \times 10^{15} \text{ cm}^{-2}$ . The samples irradiated with the fluences  $\phi \geq 10^{14} \text{ cm}^{-2}$  showed the reduction of  $\mu_0 H_c$  to 10–55% and  $M_R$  to 75–90% of the reference level.

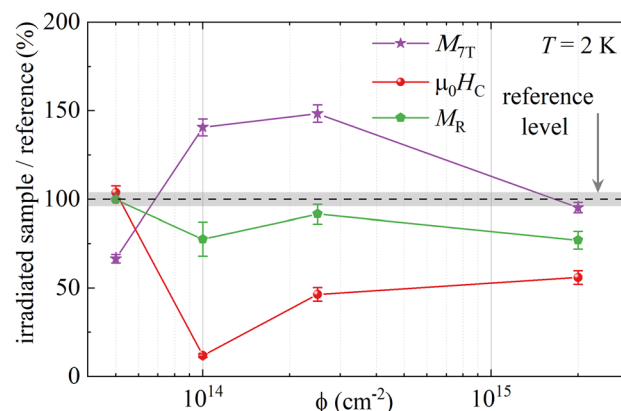


**Figure 7.** The relative values of magnetic hysteresis loop parameters for Ni(MPD)<sub>2</sub>SO<sub>4</sub> samples irradiated with various fluences  $\phi$  normalized to the reference sample's corresponding values. Violet stars: magnetization at  $\mu_0 H = 7$  T ( $M_{7T}$ ); red circles: coercive field ( $\mu_0 H_C$ ); green pentagons: remnant magnetization ( $M_R$ ). The dashed line is placed at 100% and represents the values obtained for the reference sample  $\phi = 0$  cm<sup>-2</sup> with errors indicated by gray dotted area. The lines between points are only for an eye guide.

$\Phi$ Fluence (cm <sup>-2</sup> )	$T_{irr}$		$\Delta\chi_{irr}$		$M_{7T}$		$M_R$		$\mu_0 H_C$	
	(K)	%	(emu·mol <sup>-1</sup> ·K)	%	( $\mu_B$ ·mol <sup>-1</sup> )	%	( $\mu_B$ ·mol <sup>-1</sup> )	%	(Oe)	%
0 (ref.)	21.5	100	2.09	100	0.45	100	0.025	100	1310	100
$5 \times 10^{13}$	23	107	2.84	136	0.3	67	0.025	99	1360	104
$10^{14}$	24	112	2.94	141	0.63	141	0.02	78	155	12
$2.5 \times 10^{14}$	23.5	109	2.4	115	0.69	148	0.023	92	265	46
$2.2 \times 10^{15}$	25	116	2.8	134	0.43	95	0.019	77	735	56

**Table 2.** The influence of proton irradiation on  $T_{irr}$ ,  $\Delta\chi_{irr}$ ,  $M_{7T}$ ,  $M_R$ , and  $\mu_0 H_C$  in Ni(MPD)<sub>2</sub>SO<sub>4</sub>. Absolute values and their ratio to the corresponding values for the reference sample (in percentages) are given.

## Discussion

The XRPD and IR spectroscopy measurements indicated that the core structure of Ni(MPD)<sub>2</sub>SO<sub>4</sub> remains unchanged. Consequently, the interlayer distance and the dipolar interaction are the same regardless of the fluence a sample received. Furthermore, the Curie temperature  $T_C$  remains the same because its value is determined by the weakest magnetic coupling, the dipole–dipole one. On the other hand, irradiation significantly modifies the C–H and N–H bonds, which are involved in forming hydrogen bonds related to the MPD ligand (the flexible part of the structure). In particular, the interaction of lattice with protons may lead to the C–H and N–H bonds breakage, creating hydrogen vacancies that would not be visible in XRPD, as reported in the methylammonium lead iodide perovskites after 10 MeV proton irradiation<sup>42</sup> or polymer composite of polymethyl methacrylate doped with ferric oxalate after 3 MeV proton irradiation<sup>43</sup>.

The bond modification leads to changes in the crystal field, incorporation of local defects, altered intralayer exchange couplings (due to local structure modification), and increased freedom of the magnetic moments. In consequence, magnetic properties in the LRMO phase (below  $T_C$ ) have been modified. Table 2. summarizes the influence of proton irradiation on the magnetic properties of Ni(MPD)<sub>2</sub>SO<sub>4</sub>.

The isothermal magnetization measurements (Fig. 6) confirm a strong influence of irradiation on the magnetization processes in Ni(MPD)<sub>2</sub>SO<sub>4</sub>. The main reason for this is the increasing number of defects with increasing fluence. Note that irradiating the samples with the selected fluences is not enough to obtain a homogenous distribution of produced defects, and the observed magnetization data may be a mixture of several defect-induced magnetic phases of Ni(MPD)<sub>2</sub>SO<sub>4</sub> with well-localized clusters. Introducing defects lowers the magnetostatic energy to a minimum for the dose of  $\phi = 10^{14}$  cm<sup>-2</sup> (the lowest value of the coercive field). However, a further increase in the number of defects leads to stronger pinning effects, which increase the coercive field for doses  $\phi > 10^{14}$  cm<sup>-2</sup>.

The mechanism of  $M_{7T}$  modification is different and related to changes in magnetic couplings in the compound. For the lowest dose of  $\phi = 5 \times 10^{13}$  cm<sup>-2</sup>, antiferromagnetic interactions are more dominant over the ferromagnetic ones, which lowers the magnetization  $M_{7T}$  down to 67% of the  $M_{7T}$  for the reference sample. For intermediate doses of  $\phi = 10^{14}$  cm<sup>-2</sup> and  $\phi = 2.5 \times 10^{14}$  cm<sup>-2</sup>, the corresponding values are 141% and 148%, respectively, indicating the enhancement of ferromagnetic interactions, and for the maximum dose of  $\phi = 2.2 \times 10^{15}$  cm<sup>-2</sup>, the value of  $M_{7T}$  is similar to that for the reference. Note that the calculated magnetization for the parallel alignment of Ni<sup>II</sup> magnetic moments ( $S_{Ni} = 1$ ) with a spin-only Landé factor of  $g = 2.17^{35,39}$  yields the magnetization saturation of  $M_S = 2.17 \mu_B$ ·mol<sup>-1</sup>. Thus, the antiferromagnetic interactions are dominant in all studied samples.



Similar non-monotonic effects of proton irradiation are commonly found in the literature<sup>31,33,34,44–46</sup>. In the  $\text{Ni}_{48.4}\text{Mn}_{28.8}\text{Ga}_{22.8}$  film irradiated with 120 keV protons<sup>45</sup>, the  $M_S$  for  $\phi = 10^{15} \text{ cm}^{-2}$  raised to 155% of the non-irradiated sample's value, but for  $\phi = 2 \times 10^{16} \text{ cm}^{-2}$ , the observed  $M_S$  was only 102%. Another case is the initially diamagnetic SiC (0001) single crystal<sup>44</sup> that displays ferromagnetism after 3 MeV proton irradiation treatment. For  $\phi = 8 \times 10^{15} \text{ cm}^{-2}$ , the  $M_S$  measured in-plane reached  $0.17 \text{ emu} \cdot \text{g}^{-1}$  but for  $\phi = 1.3 \times 10^{16} \text{ cm}^{-2}$  it was reduced to  $0.09 \text{ emu} \cdot \text{g}^{-1}$ .

An additional increase of the magnetization in the FC/ZFC curves observed at  $T = 2\text{--}6 \text{ K}$  for all irradiated samples may arise from a small sample's fraction, which due to the deformation and partial destruction of a lattice, leads to the creation of localized magnetic moments due to open bonds<sup>47</sup> or paramagnetic amorphous zones in the lattice<sup>44</sup>. This paramagnetic contribution may also cause the appearance of the observed step in the hysteresis loop near-zero field. The other possibility is the chemical composition modification of  $\text{Ni}(\text{MPD})_2\text{SO}_4$  samples by incorporating the highly energetic hydrogen atoms into the crystal lattice<sup>44,45</sup>. However, no additional phases were detected in the XRPD and IR measurements. Therefore, the amount of paramagnetic phase is not significant.

## Conclusions

In summary, we have investigated the impact of 1.9 MeV proton irradiation on the layered  $\text{Ni}(\text{MPD})_2\text{SO}_4$  molecular magnet in the function of received fluence  $\phi$ . It was found that proton irradiation influences only the flexible part of the structure (related to the C–H and N–H bonds in the MPD ligand), while the core of the compound remains unchanged. These lead to significant changes in magnetic properties as a function of fluence: coercive field  $\mu_0 H_c$  (reduction up to 90%), maximal magnetization  $M_T$  (between 65 and 150% of the reference sample), remanence  $M_R$  (reduction up to 25%) and degree of irreversibility  $\Delta\chi_{\text{irr}}$  (increase up to 40%). Simultaneously, the Curie temperature was constant  $T_C = 24 \text{ K}$  regardless of  $\phi$  because the core structure, interlayer distance, and, consequently, dipolar coupling of the  $\text{Ni}(\text{MPD})_2\text{SO}_4$  system remains the same. The observed non-monotonic magnetic properties changes are caused by the altered intralayer exchange couplings due to local structure modification, incorporation of local defects, and increased freedom of the magnetic moments.

## Materials and methods

**Sample preparation.** The studied  $\text{Ni}(\text{C}_6\text{H}_8\text{N}_2)_2\text{SO}_4$  compound (hereafter abbreviated as  $\text{Ni}(\text{MPD})_2\text{SO}_4$ ) was synthesized using  $\text{NiSO}_4 \cdot 7\text{H}_2\text{O}$  and 1,3-phenylenediamine (MPD,  $\text{C}_6\text{H}_8\text{N}_2$ ) ligand with a solvent-free synthesis approach according to the literature procedure<sup>35</sup>.

The Van de Graaff accelerator was used to generate a proton beam with set conditions: energy of 1.9 MeV, particle current of 10–12 nA, and beam size of about  $0.5 \text{ mm} \times 0.5 \text{ mm}$ . Powder samples mounted on copper plates were used (see Supplementary Figure S2 online) with a thickness lower than the 1.9 MeV proton penetration depth (see Supplementary Figure S3 online). The obtained fluences were equal to:  $\phi = 5 \times 10^{13} \text{ cm}^{-2}$ ,  $10^{14} \text{ cm}^{-2}$ ,  $2.5 \times 10^{14} \text{ cm}^{-2}$ ,  $2.2 \times 10^{15} \text{ cm}^{-2}$ .

**Characterization methods.** X-ray powder diffraction (XRPD) patterns were determined by the PANalytical X'Pert Pro instrument with a copper X-ray tube source ( $\text{Cu K}_{\alpha 1}$ ,  $1.541 \text{ \AA}$ ), operated at 40 kV and 30 mA in the  $\theta$ – $2\theta$  geometry. Data were recorded at room temperature in the range of  $5\text{--}40^\circ 2\theta$ . The results were adjusted by background correction and the anode's characteristic X-ray  $\text{K}_{\alpha 2}$  removal.

The infrared spectroscopy measurements were done for samples in powder form, pelleted with potassium bromide (transparent in the mid-infrared range). Fourier-transform infrared spectroscopy (FTIR) measurements were carried out in the mid-infrared range ( $4000\text{--}500 \text{ cm}^{-1}$ ), with a resolution of  $2 \text{ cm}^{-1}$ , on the EXCALIBUR 3000 spectrometer; 128 scans were done for the spectrum at room temperature.

The Quantum Design SQUID MPMS-XL magnetometer was used to measure the magnetic properties of all powder samples. The isothermal magnetization  $M(\mu_0 H)$  was collected in the applied field of  $\mu_0 H = [-7 \text{ T}, 7 \text{ T}]$ . Static magnetic susceptibility measurements were carried out in the field cooling (FC) and zero-field cooling (ZFC) modes in the  $T = 2.0\text{--}300 \text{ K}$  temperature range with the applied field of  $\mu_0 H_{\text{dc}} = 0.01 \text{ T}$ . The obtained data points were processed taking the whole sample mass, i.e., assuming a homogeneous distribution of potential changes in the studied compounds after proton irradiation. The temperature-independent diamagnetic contribution of  $\chi_0 = -1.84 \times 10^{-4} \text{ emu} \cdot \text{mol}^{-1}$  estimated from Pascal's constants<sup>48</sup> was subtracted from the measured signals.

## Data availability

The datasets used and/or analyzed during the current study are available from the corresponding author on reasonable request.

Received: 28 March 2023; Accepted: 22 August 2023

Published online: 28 August 2023

## References

1. Raman, K. V. *et al.* Interface-engineered templates for molecular spin memory devices. *Nature* **493**, 509–513 (2013).
2. Aguilà, D. *et al.* Heterodimetallic  $[\text{LnLn}']$  lanthanide complexes: Toward a chemical design of two-qubit molecular spin quantum gates. *J. Am. Chem. Soc.* **136**, 14215–14222 (2014).
3. Pedersen, K. S. *et al.* Toward molecular 4f single-ion magnet qubits. *J. Am. Chem. Soc.* **138**, 5801–5804 (2016).
4. Coronado, E. Molecular magnetism: From chemical design to spin control in molecules, materials and devices. *Nat. Rev. Mater.* **5**, 87–104 (2020).
5. Song, T. Q. *et al.* Wheel-like  $\text{Ln}_{18}$  cluster organic frameworks for magnetic refrigeration and conversion of  $\text{CO}_2$ . *Inorg. Chem.* **57**, 3144–3150 (2018).

6. Zheng, X. Y., Kong, X. J., Zheng, Z., Long, L. S. & Zheng, L. S. High-nuclearity lanthanide-containing clusters as potential molecular magnetic coolers. *Acc. Chem. Res.* **51**, 517–525 (2018).
7. Wang, W. M. *et al.* Large magnetocaloric effect and remarkable single-molecule-magnet behavior in triangle-assembled  $\text{Ln}^{\text{III}}$  clusters. *New J. Chem.* **43**, 16639–16646 (2019).
8. Konieczny, P. *et al.* Magnetic cooling: A molecular perspective. *Dalt. Trans.* **51**, 12762–12780 (2022).
9. Korzeniak, T. *et al.* Chiral photomagnets based on Copper(II) complexes of 1,2-Diaminocyclohexane and Octacyanidomolybdate(IV) Ions. *Inorg. Chem.* **59**, 5872–5882 (2020).
10. Jiang, W. *et al.* Switching single chain magnet behavior: Via photoinduced bidirectional metal-to-metal charge transfer. *Chem. Sci.* **9**, 617–622 (2018).
11. Yue, Q. & Gao, E. Q. Azide and carboxylate as simultaneous coupler for magnetic coordination polymers. *Coord. Chem. Rev.* **382**, 1–31 (2019).
12. Pedersen, K. S., Bendix, J. & Clérac, R. Single-molecule magnet engineering: Building-block approaches. *Chem. Commun.* **50**, 4396–4415 (2014).
13. Vallone, S. P. *et al.* Giant barocaloric effect at the spin crossover transition of a molecular crystal. *Adv. Mater.* **31**, 1–7 (2019).
14. Bridonneau, N. *et al.* Direct evidence of a photoinduced electron transfer in diluted “molybdenum-copper” molecular compounds. *Eur. J. Inorg. Chem.* **2018**, 370–377 (2018).
15. Makgato, T. N. *et al.* Magnetic properties of point defects in proton irradiated diamond. *J. Magn. Magn. Mater.* **413**, 76–80 (2016).
16. Esquinazi, P. *et al.* Induced magnetic ordering by proton irradiation in graphite. *Phys. Rev. Lett.* **91**, 8–11 (2003).
17. Kasper, C. *et al.* Influence of irradiation on defect spin coherence in silicon carbide. *Phys. Rev. Appl.* **13**, 1 (2020).
18. Yang, Z. P., Tan, C. L., Gao, Z. Y., Gao, Y. & Cai, W. Effect of proton irradiation on microstructural and magnetic properties of ferromagnetic Ni–Mn–Ga thin films. *Thin Solid Films* **632**, 10–16 (2017).
19. Ghigo, G. *et al.* Effects of proton irradiation on the magnetic superconductor  $\text{EuFe}_2(\text{As}_{1-x}\text{P}_x)_2$ . *Supercond. Sci. Technol.* **33**, 94011 (2020).
20. Patki, P. V., Wu, Y. & Wharry, J. P. Effects of proton irradiation on microstructure and mechanical properties of nanocrystalline Cu–10at%Ta alloy. *Materialia* **9**, 100597 (2020).
21. Smith, K. A. *et al.* Effect of proton irradiation on anatase  $\text{TiO}_2$  nanotube anodes for lithium-ion batteries. *J. Mater. Sci.* **54**, 13221–13235 (2019).
22. Smith, K. A. *et al.* Effects of proton irradiation on structural and electrochemical charge storage properties of  $\text{TiO}_2$  nanotube electrodes for lithium-ion batteries. *J. Mater. Chem. A* **5**, 11815–11824 (2017).
23. Dutta, T. *et al.* Non-destructive patterning of 10 nm magnetic island array by phase transformation with low-energy proton irradiation. *Appl. Phys. Lett.* **111**, 1–6 (2017).
24. Kim, S. *et al.* Nanoscale patterning of complex magnetic nanostructures by reduction with low-energy protons. *Nat. Nanotechnol.* **7**, 567–571 (2012).
25. Avasthi, D. K. & Mehta, G. K. *Swift Heavy Ions for Materials Engineering and Nanostructuring* (Springer Series in Materials Science (Springer), 2011).
26. Esquinazi, P. D. *et al.* Defect-induced magnetism in nonmagnetic oxides: Basic principles, experimental evidence, and possible devices with ZnO and  $\text{TiO}_2$ . *Phys. Status Solidi Res.* **257**, 1900623 (2020).
27. Zhou, R. W., Liu, X. C., Li, F. & Shi, E. W. Defects induced ferromagnetism in hydrogen irradiated 3C–SiC thin films. *Mater. Lett.* **156**, 54–57 (2015).
28. Hassan, N. U. *et al.* Influence of ion beam irradiation on structural, magnetic and electrical characteristics of ho-doped AlN thin films. *Surf. Rev. Lett.* **24**, 1–7 (2017).
29. Matsushita, M., Matsushima, Y., Uruga, T., Ishigami, R. & Iwase, A. Effect of 50-keV proton irradiation on the magnetism of a  $\text{Fe}_{66}\text{Ni}_{34}$  Invar alloy. *J. Magn. Magn. Mater.* **333**, 13–17 (2013).
30. Matsushita, M., Wada, H. & Matsushima, Y. Effects of fluence and fluence rate of proton irradiation upon magnetism in  $\text{Fe}_{65}\text{Ni}_{35}$  Invar alloy. *J. Magn. Magn. Mater.* **394**, 491–495 (2015).
31. Kim, S. J., Lee, K. J., Jung, M. H., Oh, H. J. & Kwon, Y. S. Magnetocaloric effect in  $\text{la}(\text{Fe}_{0.89}\text{Si}_{0.11})_{13}$  irradiated by protons. *J. Magn. Magn. Mater.* **323**, 1094–1097 (2011).
32. Jiang, X. D. *et al.* Influence of the interface on the magnetic properties of NiZn ferrite thin films treated by proton irradiation. *Nucl. Instrum. Methods Phys. Res. Sect. B Beam. Interact. Mater. Atoms.* **358**, 1–5 (2015).
33. Jeon, G. W., Lee, K. W. & Lee, C. E. High-energy proton-irradiation effects on the magnetism of the transition-metal dichalcogenide  $\text{MoS}_2$ . *J. Korean Phys. Soc.* **76**, 93–96 (2020).
34. Mathew, S. *et al.* Magnetism in  $\text{MoS}_2$  induced by proton irradiation. *Appl. Phys. Lett.* **101**, 102103 (2012).
35. González Guillén, A. B. *et al.* Tuning magnetic properties by crystal engineering in a family of coordination polymers based on Ni(II) sulphates. *New J. Chem.* **46**, 14786–14792 (2022).
36. Dijks, I. J., De Koning, R., Geus, J. W. & Jenneskens, L. W. Anhydrous zirconium(IV) sulfate and tin(IV) sulfate: Solid Lewis acid catalysts in liquid-phase hydro-acyloxy-addition reactions?. *Phys. Chem. Chem. Phys.* **3**, 4423–4429 (2001).
37. Nakagawa, I. & Shimanouchi, T. Infrared spectroscopic study on the co-ordination bond-II. *Spectrochim. Acta* **18**, 101–113 (1962).
38. Yao, W., Yu, S.-H., Jiang, J. & Zhang, L. Complex wurtzite znse microspheres with high hierarchy and their optical properties. *Chem. A Eur. J.* **12**, 2066–2072 (2006).
39. Pinkowicz, D. *et al.* Nature of magnetic interactions in 3D  $\{[\text{MII}(\text{pyrazole})_4]_2[\text{NBIV}(\text{CN})_8] \cdot 4\text{H}_2\text{O}\}_n$  ( $\text{M} = \text{Mn, Fe Co, Ni}$ ) molecular magnets. *Inorg. Chem.* **49**, 7565–7576 (2010).
40. Dubiel, S. M. & Felner, I. On the magnetism of  $\text{C}_{14}\text{Nb}(\text{Fe}_{89.4}\text{Al}_{10.6})_2$  laves phase intermetallic compound. *Epl* **128**, 27005 (2019).
41. Dubiel, S. M., Felner, I. & Tsindlekht, M. I. Magnetic phase diagram of sigma-phase  $\text{Fe}_{55}\text{Re}_{45}$  compound in the H-T coordinates. *J. Appl. Phys.* **126**, 154 (2019).
42. Shin, J. *et al.* Proton irradiation effects on mechanochemically synthesized and flash-evaporated hybrid organic–inorganic lead halide perovskites. *Nanotechnology* **33**, 065706 (2022).
43. Shah, S., Qureshi, A., Singh, N. L., Singh, K. P. & Ganesan, V. Modification of polymer composite by proton beam irradiation. *Soft Mater.* **6**, 75–84 (2008).
44. He, X. *et al.* Irradiation-induced magnetic ordering in SiC: Experimental results and a density functional study. *Appl. Phys. Lett.* **103**, 262409 (2013).
45. Yang, Z. P., Sun, B., Gao, Z. Y. & Cai, W. Surface modifications and tailoring magnetism in  $\text{Ni}_{48.4}\text{Mn}_{28.8}\text{Ga}_{22.8}$  films by 120 keV proton irradiation. *Intermetallics* **98**, 106–114 (2018).
46. Liu, Y. *et al.* Towards diluted magnetism in TaAs. *Phys. Rev. Mater.* **1**, 044203 (2017).
47. Stöfler, D., Drescher, M., de Jauregui, D. S., Gmeiner, J. & Dormann, E. Proton irradiation defects in (fluoranthene) $_2\text{PF}_6$ . *Phys. Lett. A* **363**, 317–321 (2007).
48. Bain, G. A. & Berry, J. F. Diamagnetic corrections and Pascal's constants. *J. Chem. Educ.* **85**, 532–536 (2008).

## Acknowledgements

We thank O. Polit for assistance in part of the correct sample preparation. This work was supported by the Polish Minister of Education and Science (G. No.: DI2017 006047).



### Author contributions

D.C.: study design, magnetic properties data collection, analysis, and interpretation, manuscript preparation; P.K.: data interpretation, manuscript preparation; E.J.G.: infrared spectroscopy data collection and analysis, manuscript preparation; M.P.: powder X-ray data collection and analysis; J.L.: proton irradiation; A.B.G.G. and W.L.: sample synthesis, structure details, manuscript revision.

### Competing interests

The authors declare no competing interests.

### Additional information

**Supplementary Information** The online version contains supplementary material available at <https://doi.org/10.1038/s41598-023-41156-8>.

**Correspondence** and requests for materials should be addressed to D.C. or P.K.

**Reprints and permissions information** is available at [www.nature.com/reprints](http://www.nature.com/reprints).

**Publisher's note** Springer Nature remains neutral with regard to jurisdictional claims in published maps and institutional affiliations.



**Open Access** This article is licensed under a Creative Commons Attribution 4.0 International License, which permits use, sharing, adaptation, distribution and reproduction in any medium or format, as long as you give appropriate credit to the original author(s) and the source, provide a link to the Creative Commons licence, and indicate if changes were made. The images or other third party material in this article are included in the article's Creative Commons licence, unless indicated otherwise in a credit line to the material. If material is not included in the article's Creative Commons licence and your intended use is not permitted by statutory regulation or exceeds the permitted use, you will need to obtain permission directly from the copyright holder. To view a copy of this licence, visit <http://creativecommons.org/licenses/by/4.0/>.

© The Author(s) 2023